Applied Surface Science 256 (2010) 1895–1907

Contents lists available at ScienceDirect

Applied Surface Science

journal homepage: www.elsevier.com/locate/apsusc

Effects of annealing on properties of ZnO thin films prepared by electrochemical deposition in chloride medium

O. Lupan [a,b,*], T. Pauporté [a,**], L. Chow [c,d], B. Viana [e], F. Pellé [e], L.K. Ono [c], B. Roldan Cuenya [c,f], H. Heinrich [c,d]

[a] Laboratoire d'Electrochimie, Chimie des Interfaces et Modélisation pour l'Energie (LECIME), UMR 7575 CNRS, Chimie ParisTech, 11 rue P. et M. Curie, 75231 Paris Cedex 05, France
[b] Department of Microelectronics and Semiconductor Devices, Technical University of Moldova, 168 Stefan cel Mare Blvd., Chisinau MD-2004, Republic of Moldova
[c] Department of Physics, University of Central Florida, PO Box 162385, Orlando, FL 32816-2385, USA
[d] Advanced Materials Processing and Analysis Center, and Department of Mechanical, Materials, and Aerospace Engineering, University of Central Florida, PO Box 162385 Orlando, FL 32816-2455, USA
[e] Laboratoire de Chimie de la Matière Condensée de Paris, UMR 7574-CNRS- Chimie ParisTech -UPMC, 11 rue P. et M. Curie, 75231 Paris Cedex 05, France
[f] Department of Civil, Environmental and Construction Engineering, and Nanoscience Technology Center, University of Central Florida, Orlando, FL, USA

ARTICLE INFO

Article history:
Received 27 July 2009
Received in revised form 10 October 2009
Accepted 10 October 2009
Available online 20 October 2009

Keywords:
ZnO
Thin films
Electrodeposition
Photoluminescence
Annealing

ABSTRACT

The development of cost-effective and low-temperature synthesis techniques for the growth of high-quality zinc oxide thin films is paramount for fabrication of ZnO-based optoelectronic devices, especially ultraviolet (UV)-light-emitting diodes, lasers and detectors. We demonstrate that the properties, especially UV emission, observed at room temperature, of electrodeposited ZnO thin films from chloride medium (at 70 °C) on fluor-doped tin oxide (FTO) substrates is strongly influenced by the post-growth thermal annealing treatments. X-ray diffraction (XRD) measurements show that the films have preferably grown along (0 0 2) direction. Thermal annealing in the temperature range of 150–400 °C in air has been carried out for these ZnO thin films. The as-grown films contain chlorine which is partially removed after annealing at 400 °C. Morphological changes upon annealing are discussed in the light of compositional changes observed in the ZnO crystals that constitute the film. The optical quality of ZnO thin films was improved after post-deposition thermal treatment at 150 °C and 400 °C in our experiments due to the reducing of defects levels and of chlorine content. The transmission and absorption spectra become steeper and the optical bandgap red shifted to the single-crystal value. These findings demonstrate that electrodeposition have potential for the growth of high-quality ZnO thin films with reduced defects for device applications.

© 2009 Elsevier B.V. All rights reserved.

1. Introduction

Zinc oxide (ZnO) is a II–VI group semiconductor material with a hexagonal Wurtzite crystal structure [1,2], a wide and direct bandgap of 3.37 eV (at 300 K), a large free-exciton binding energy (60 meV) [3], a strong cohesive energy of 1.89 eV [4], a high optical gain (300 cm^{-1}) [5], high mechanical and thermal stabilities [6], and radiation hardness [7–9]. ZnO possesses a Wurtzite structure similar to GaN [10,11], which is widely used in high-performance optoelectronic devices. ZnO is a promising candidate material for advanced devices applications due to the above-mentioned characteristics and unique combination of its physical properties—optical, electrical, magnetic, piezoelectric, and ferroelectric. Due to these unique characteristics it is expected ZnO's efficient utilization in different commercial applications such as integrated optics, antireflection coatings, liquid crystal displays [10], light-emitting diodes [12,13], laser diodes [13], UV range detecting devices [14,15], chemical sensors [16,17], solar cells [18,19], photodegradation and photocatalysis [20], superhydrophobic and self-cleaning surfaces [21]. ZnO is also a strong candidate for high temperature electronic devices that can reliably be operated in space and other harsh environments [7,8].

ZnO thin films have been synthesized by a variety of processes, including vapor deposition [22], pulsed laser deposition [23], molecular beam epitaxy [24], metal organic chemical vapor deposition (MOCVD) [25], sputtering [26], electron beam evaporation [27], spray pyrolysis [28], sol–gel processing [29], chemical [16,18,30], and electrochemical deposition [31–40]. Among these, electrochemical deposition (ECD) is known to be a simple, low temperature, and cost-effective large-area deposition technique for

* Corresponding author at: Laboratoire d'Electrochimie, Chimie des Interfaces et Modélisation pour l'Energie (LECIME), UMR 7575 CNRS, Chimie ParisTech, 11 rue P. et M. Curie, 75231 Paris Cedex 05, France.
** Corresponding author.
E-mail addresses: oleg-lupan@enscp.fr, lupanoleg@yahoo.com (O. Lupan), thierry-pauporte@enscp.fr (T. Pauporté).

0169-4332/$ – see front matter © 2009 Elsevier B.V. All rights reserved.
doi:10.1016/j.apsusc.2009.10.032

group II–VI semiconductors such as ZnO. High-quality ZnO films grown by ECD have been reported [34–40], which can be easily scaled up for optoelectronic devices fabrications. However, several issues have to be clarified. It is well known that in order to obtain a high-quality ZnO films by ECD, it is necessary to employ a supporting electrolyte to ensure a good electrical conduction during electroplating [34,35]. In most of the reported works, potassium chloride (KCl) with concentration of 0.1 M was employed as a supporting electrolyte to ensure a good conductivity in aqueous solution [34–40]. The chloride content is typically much higher (more than 20 times) than zinc content in the solution. A very important issue in ECD of ZnO thin films is the effect of Chlorine (Cl^-) ions on the structural and optical properties of ZnO thin films and how it could affect the device performance and reliability. Another issue is the effect of thermal annealing on these ECD ZnO thin films grown from chloride medium and how it influences Cl^- ions contained in ZnO thin films. Answers to these questions are extremely important for further improvements of ECD techniques, because the thin films properties are determined by the phenomena at the atomic level and by crystallographic uniformity, which ensure stable function of future devices based on.

It has been shown that Cl^- is incorporated in a rather large amount in ZnO upon electrodeposition in KCl medium at relatively low temperature [35,38,40]. The amount decreases with an increase in the deposition temperature [35]. Only a few reports [35,38–43] on chloride doping in ZnO thin films have been published. Chikoidze et al. [41,42] reported on the effect of chlorine doping on electrical and optical properties of ZnO thin films grown by MOCVD. The effect of thermal annealing on ECD ZnO is also poorly documented. Pauporté and Lincot have shown [40] the marked effects of annealing on the structural and optical properties of the films. Laurent et al. [37] reported the effect of thermal annealing in Ar atmosphere on optical properties of ECD ZnO thin films on gilded silicon substrate.

In this work, we report on the fabrication and a detailed investigation of the effect of annealing on properties of ECD ZnO thin films from chloride medium. An in-deep analysis of Cl^- ions content in ZnO films including depth distribution and annealing behavior is reported. Improvements of optical and structural properties were observed after annealing at 150 °C and 400 °C. These results represent a meaningful step toward fabrication of ZnO thin films light-emitting diodes (LED).

2. Experimental details

2.1. Electrochemical deposition

ZnO thin films were prepared by the electrochemical deposition (ECD) method from a 5 mM $ZnCl_2$ (Merk, 99%) aqueous solution maintained at 70 °C as reported before [35]. For supporting electrolyte, 0.1 M of potassium chloride (KCl) (Fluka 98%) was employed to ensure a good conductivity in the aqueous solution. The ZnO film was grown on the conductive F-doped tin oxide (FTO) film deposited on a glass substrate with a sheet resistance of 10 Ω/□. FTO substrate was used as working electrode (WE) in a classical three electrode cell for electrochemical deposition. Before deposition, the substrates were cleaned in acetone, then ethanol (95%) for 5 min each in the ultrasonic bath, followed by rinsing with abundant deionized (DI) water (18.2 MΩ cm) flow. Afterwards, the substrates were immersed in HNO_3 (45%) for 2 min and finally cleaned in deionized (DI) water in the ultrasonic bath for 2 min and dried in air flux. Cleaned FTO substrate was mounted on a working electrode. Contacts were performed with Cu wire and at the end by In-Ga eutectic to ensure good conductivity between WE and FTO and checked from *I*–*V* measurements. The reference electrode (RE) was a saturated calomel electrode (SCE) with a potential at +0.25 V vs. NHE (normal hydrogen electrode) which was placed in a separated compartment maintained at room temperature. A platinum (Pt) spiral wire was used as the counter electrode (CE). The distance between FTO working electrode and counter electrode was 3 cm and 3.5 cm between the RE and WE. Electrodeposition was carried out potensiostatically at −1.0 V using an Autolab PGSTAT30 potentiostat/galvanostat without stirring, but with rotation of WE (with constant speed of ω = 300 rotations/min (rpm)). The potentiostat was monitored by the AutoLab software. The pH of the solutions was initially 5.5. The single compartment electrochemical cell was mounted in a thermoregulated bath and the temperature was fixed at 70 °C with an uncertainty of ±0.2 °C. The electrolyte was saturated with pure oxygen by bubbling for 45 min prior to electrolysis start and continuously kept on during the growth process. The growing process ended in 20 min when the total passed/exchanged electrical charge reached 1.0 C cm^{-2}. In the case of a faradic efficiency equal to 1, this charge corresponds to a dense film thickness of 820 nm [35], however in our experiments we have grown a film of 800 nm, so faradic efficiency equals to about 0.975.

Fundamental physicochemical properties of cathodic ZnO synthesis in an aqueous zinc chloride solution of $[ZnCl_2]$ = 5 mM and the formation of hydroxide ions from oxygen and water can be described as follows [43]:

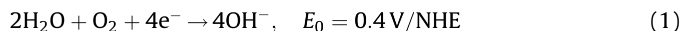

$$2H_2O + O_2 + 4e^- \rightarrow 4OH^-, \quad E_0 = 0.4\,V/NHE \tag{1}$$

ZnO films are electrodeposited according to the overall reaction [43]:

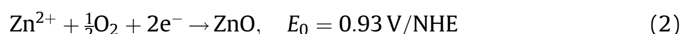

$$Zn^{2+} + \tfrac{1}{2}O_2 + 2e^- \rightarrow ZnO, \quad E_0 = 0.93\,V/NHE \tag{2}$$

The films were deposited at a constant applied potential (−1.0 V), and the variation of current density, *j*, with time was recorded. Fig. 1 represents the variation of current density with time for ECD of ZnO films on FTO substrate at 70 °C, *E* = −1 V/SCE with rotating WE (300 rpm).

The illustrated curve (Fig. 1) confirms that the ECD ZnO thin films are good electrical conductors, as the current density collected at the electrode is kept at a significant value. Steady state *j* of pure ZnO is about 0.77 mA cm^{-2} after 180 s of growth. An important feature of the curve in Fig. 1 is the presence of a cathodic wave at low deposition time (<200 s), which is assigned to the nucleation–growth process of the ZnO thin film before it fully covers the FTO substrate [40]. The presence of this wave is typically observed for films of good crystallographic quality and coverage [35,37,40,44].

After the electrodeposition, zinc oxide thin films were rinsed with DI water, to remove chloride salts and un-reacted products

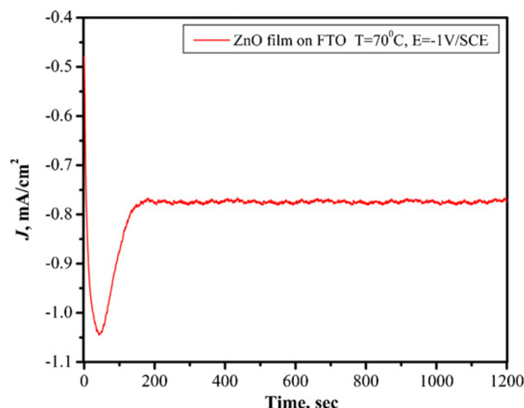

Fig. 1. Variation of current density with time during of ECD of ZnO films on FTO substrate at 70 °C, *E* = −1 V/SCE with rotating WE (ω = 300 rpm).

from the surface of the films. ECD ZnO thin films were dried in a moderate air flux, and then sample was cut in four similar parts. One was used as reference and three others samples were annealed using a tubular furnace at 150 °C for 5 h, 400 °C for 1 h and 600 °C for 1 h in air, respectively. Thus, in order to observe the influence of annealing on the ZnO thin film these three samples electrochemically grown in chloride medium exactly in the same conditions were used. The first annealing treatment (150 °C) was chosen as compatible with light-weight plastic flexible substrates.

2.2. Characterization of electrochemical deposited ZnO thin films

XRD was carried out using Siemens D5000 XRD unit (with 40 kV and 45 mA, Cu Kα radiation with λ = 1.5406 Å). The average dimension of crystallites and lattice strain were determined by the Scherrer method [45] from the broadening and shift of the diffraction peaks taking into account the instrumental broadening.

SEM micrographs were observed with a high-resolution Ultra 55 Zeiss FEG scanning electron microscope at an acceleration voltage of 10 kV. Energy dispersive X-ray spectroscopy (EDX) analyses were realized with a Bruker Li-drift silicon detector.

The ex-situ prepared samples were subsequently transferred into an ultrahigh vacuum system (UHV) for electronic/chemical characterization. All in-situ investigations were performed in a modular UHV system (SPECS GmbH) specially designed for the preparation and characterization of nanoscaled materials. The analysis chamber was equipped with a hemispherical electron energy analyzer (Phoibos 100) and dual-anode (Al Kα, 1486.6 eV and Ag Lα, 2984.4 eV) monochromatic X-ray source (XR50, SPECS GmbH) for X-ray photoelectron spectroscopy (XPS). The base pressure in this chamber is $1–2 \times 10^{-10}$ mbar. In our studies, Al Kα radiation was used. Details of the experimental procedures can be found in our previous reports [46].

Secondary Ion Mass Spectrometry (SIMS) was used for the analysis of the Cl content because of its excellent sensitivity and depth resolution [47]. SIMS measurements were carried out with a Physical Electronics ADEPT 1010 quadrupole analyzer with a 3 keV Cs^+ primary beam at 60° from normal. The typical primary beam current was 25 nA. The primary beam was rastered over a 300 μm by 300 μm area, with detection of negative secondary ions from an area of 100 μm by 100 μm at the center of the rastered area.

A TEM cross-sectional sample was prepared using a Focused Ion Beam (FIB) system FEI 200. The micro-manipulator inside the FIB chamber is used to pick up the TEM cross-sectional sample and to mount it on a Cu grid. Transmission electron microscopy (TEM) and selected-area electron diffraction (SAED) measurements were performed on a FEI Tecnai F30 TEM transmission electron microscope operating at an accelerating voltage of 300 kV.

Raman scattering measurements was performed at room temperature with a Horiba Jobin Yvon LabRam IR system in a backscattering configuration. A 632.8 nm line of a He-Ne laser was used for off-resonance excitation with less than 4 mW power at the sample. The instrument was calibrated to the same accuracy using silicon and a naphthalene standard.

A Dektak 6M Stylus Profiler was used to determine film thickness after making a step in the film by etching. Specular transmittance measurements were performed at room temperature with unpolarized light at normal incidence in the wavelength range from 300 nm to 850 nm using Cary 50 (Varian) UV–Vis-NIR spectrophotometer. The reference was a FTO coated glass substrate cleaned exactly with the same procedure. Reflectance measurements were investigated at an angle of incidence of 7° in the same wavelength range. The diffuse reflectance spectra were measured on a Varian Cary 5E UV–Vis-NIR spectrophotometer equipped with an integrating sphere. The optical absorption coefficient α was calculated from the transmittance and reflectance data by using the equation [48]:

$$T = (1 - R)^2 \exp(-\alpha t) \tag{3}$$

where T is transmittance, R is reflectance, and t is the film thickness.

The absorption coefficient α is related to the incident photon energy $h\nu$ as

$$\alpha = \frac{K(h\nu - E_g)^{n/2}}{h\nu} \tag{4}$$

where K is a constant which is function of refractive index of the material, reduced mass and speed of light, E_g is the optical bandgap, and n is equal to 1 for direct bandgap material such as ZnO. Using the above relationship the bandgap was evaluated by plotting $(\alpha h\nu)^2$ as a function of incident radiation $h\nu$ and then extrapolating the straight linear part to the curve and intercept with energy axis, according to the procedure reported before [30].

Photoluminescence (PL) was measured in the temperature range from 9 K to 300 K using a helium cryostat [35]. The samples were mounted on the cold station of a LTS-22-C-330 optical cryogenic system. The continuous wave (CW) photoluminescence (PL) was excited by the 4th harmonic (266 nm) of an YAG:Nd laser and dispersed with a HR250 monochromator (Jobin–Yvon) coupled to an UV-enhanced Intensified Charge Coupled Device (ICCD) (Roper). Under pulsed laser excitation, PL spectra were recorded in a pseudo CW mode with a continuous integration of the intensity in 300 ms corresponding to 3 full illumination pulses. The excitation power and the geometrical arrangement of the experiment was kept the same for all studies. All spectra were normalized using the emission of the same electrodeposited ZnO film as a reference (grown at −1 V vs. SCE, temperature 85 °C, 5 mM $ZnCl_2$ and 0.1 M KCl, Q_{tot} = 1.1 C cm^2, same sample as in Ref. [35]). Thus, all experimental conditions being the same, the emission intensities can be compared in a quantitative way.

3. Results and discussions

3.1. Structural and morphological characterizations of ZnO thin films

Fig. 2 shows the effects of thermal annealing temperature on the crystallinity of the ECD ZnO thin films on FTO substrate. All dot (red on-line) marked peaks are assigned to SnO_2 according to PDF 01-077-0488 card [49]. It can be seen that electrodeposited ZnO films shows sharp XRD reflection peak detected at ∼34.4°, suggesting that the growth is along the c-axis normal to the substrate. The intensity of the peaks relative to the background demonstrates high purity of the hexagonal ZnO phase and good crystallinity of the samples. The XRD patterns from the as-grown ECD ZnO film and annealed at 150 °C (Fig. 2a and b) indicate a (0 0 2)-preferred orientation, which suggests that the film is aligned with the c-axis oriented perpendicularly to the substrate surface. In Fig. 2a, the strongest detected ($h\,k\,l$) peak was observed at 2θ values of 34.34°, corresponding to the lattice plane (0 0 2) in ZnO. The ZnO peaks of much lower intensity were also detected at 31.7°, 36.2°, 47.5°, 56.6°, and 62.8° ($(I_{0\,0\,2})/(I_{h\,k\,l}) > 38$) corresponding to the following lattice planes: (1 0 0), (1 0 1), (1 0 2), (1 1 0), (1 0 3), respectively.

From Fig. 2b, it can be seen that the intensity as well as full-width-half-maximum (FWHM) of (0 0 2) peak is dependent on annealing temperatures and the film remains highly oriented with the c-axis normal to the substrate. Intensity reaches the maximum value after annealing at 400 °C for 1 h comparing with as-grown sample or thermally treated one at 150 °C for 5 h. The position of the (0 0 2) peaks (see Fig. 2 and Table 1) is shifted to a higher 2θ

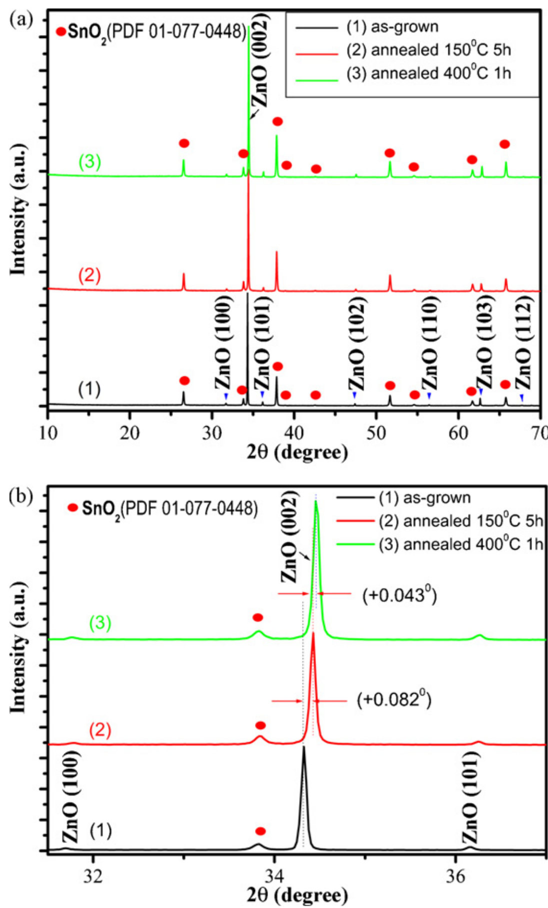

Fig. 2. (a) XRD spectra of ZnO films grown by electrochemical method in chloride medium at 70 °C. (b) Position of XRD (0 0 2) peak and intensity with various annealing temperatures of ECD ZnO thin films.

values from initial 34.34° (as-grown) to 34.42° and 34.47° after annealing at 150 °C and 400 °C, respectively. The shift of XRD peak (0 0 2) towards higher angle as increasing annealing temperature was reported previously [37,40,50,51]. This could be due to the release of intrinsic strain through annealing [37,52]. For example, the lattice parameter d (0 0 2) in the un-stress ZnO bulk is about 2.602 Å, and the d (0 0 2) value of as-grown ECD ZnO films is 2.611 Å and after annealing at 150 °C is 2.603 Å. These values suggest that the stress is released after annealing. More details are presented in Table 1. It is known that microstrain is due to imperfections within the crystalline lattice, including vacancies, stacking faults, interstitials, etc. According to our calculations by using Scherrer method [53] lattice strain is 0.158% in as-grown film and only 0.105% in annealed samples. The full-width-half-maximum (FWHM) values of (0 0 2) peak of ZnO films on FTO substrate are 0.1248°, 0.0936° and 0.0930° (Fig. 2b and Table 1) for the as-deposited and after annealing at 150 °C and 400 °C, respectively. These reasonably narrow FWHM widths (see Fig. 2) demonstrate the high crystal quality of ZnO films obtained by electrochemical deposition on FTO substrates.

The sample annealed at 150 °C, showed a slight change in intensity of (0 0 2) diffraction peak (Fig. 2b and Table 1). This implies that the crystallite quality hardly changed after annealing at 150 °C for 5 h. However, as the annealing temperature is further increased to 400 °C, the intensity of (0 0 2) peak is increased by a factor of 1.21 (Fig. 2b and Table 1). This can be explained by improvement of crystallinity or it can also be attributed to the changes of Cl atoms content in the ECD ZnO film as will be discussed in the following sections.

A relationship between the intensity of dominant (0 0 2) XRD diffraction peak, which tends to increase slightly with annealing temperature at 150 °C and increases markedly at 400 °C and also FWHM and other parameters are shown in Table 1.

As ZnO crystallizes in the Wurtzite structure in which the oxygen atoms are arranged in a hexagonal closed-packed type (*hcp*) with zinc atoms occupying half the tetrahedral sites. Zn and O atoms are tetrahedrally coordinated to each other and have, therefore, an equivalent position. The zinc structure is open with all the octahedral and half the tetrahedral sites empty. The lattice constants a and c of Wurtzite structure ZnO were calculated, according to Bragg's law [45]:

$$n\lambda = 2d\sin\theta \tag{5}$$

where n is the order of diffraction (usually $n = 1$), λ is the X-ray wavelength and d is the spacing between planes of given Miller indices h, k and l. In the ZnO hexagonal structure, the plane spacing is related to the lattice constants a, c and the Miller indices by the following relation [45]:

$$\frac{1}{d^2_{(hkl)}} = \frac{4}{3}\left(\frac{h^2+hk+k^2}{a^2}\right) + \frac{l^2}{c^2}, \tag{6}$$

with the first order approximation, $n = 1$:

$$\sin^2\theta = \frac{\lambda^2}{4a^2}\left[\frac{4}{3}(h^2+k^2+hk) + \left(\frac{a}{c}\right)^2 l^2\right], \tag{7}$$

$$a = \frac{\lambda}{2\sin\theta}\sqrt{\frac{4}{3}\left(h^2+hk+\frac{L^2}{(c/a)^2}\right)}, \tag{8a}$$

$$c = \frac{\lambda}{2\sin\theta}\sqrt{\frac{4}{3(a/c)^2}(h^2+hk+L^2)}, \tag{8b}$$

for the (1 0 0) orientation at 2θ = 31.699°, 31.776°, and 31.777°, the lattice constant a was calculated by

$$a = \frac{\lambda}{\sqrt{3}\sin\theta} \tag{9}$$

Table 1
Effect of annealing in air on structural properties of electrodeposited ZnO thin films.

Annealing temperature (°C)	X-ray intensity of diffraction peak (002) relative to of as-grown films	XRD (002) peak position (°)	FWHM XRD (002) peak [2θ°]	d (Å) (002)	a (Å) (100)	c (Å) (002)	TC (002) texture coefficient	[Cl]:[Zn] ratio by EDX
				Un-stress ZnO bulk 2.602	Pure ZnO 3.2498	Pure ZnO 5.2066		
As-grown	1.00	34.34°	0.1248°	2.611	3.2568	5.2194	3.2	0.0319
150 °C	1.05	34.42° (+0.08°)	0.0936°	2.603	3.2489	5.2063	4.2	0.0344
400 °C	1.21	34.47° (+0.05°)	0.0930°	2.601	3.2489	5.2021	3.6	0.0248

for the (0 0 2) orientation at $2\theta = 34.42^\circ$, the lattice constant c was calculated by

$$c = \frac{\lambda}{\sin\theta} \quad (10)$$

The lattice constants a and c were determined as $a = 3.2498$ Å and $c = 5.2066$ Å for pure ZnO [54]. However, for the as-grown ECD ZnO films: $a = 3.2568$ Å and $c = 5.2184$ Å, which demonstrates an expansion of the lattice parameter. Slightly increase for both 'a' and 'c' parameters in our samples could be possible due to the Cl^- content or its incorporation in ZnO structure/film [35,37,40,55]. A small increase in the lattice parameters would be expected when O^- ions are replaced by Cl^- ions because of the larger ionic radius of Cl^- ($r(Cl^-) = 0.181$ nm), than O^- ($r(O^-) = 0.140$ nm) and Zn^{2+} ($r(Zn^{2+}) = 0.074$ nm), respectively [56,57]. The increase in the lattice parameters could also be caused by interstitial incorporation of Cl^- ions into the lattice.

Lower values of a and c were found ($a = 3.2489$ Å, $c = 5.20634$ Å) for ECD ZnO films annealed at 150 °C, which are very close to the pure bulk ZnO. After annealing ECD ZnO at 400 °C in air, the lattice constants become even lower $a = 3.2489$ Å, $c = 5.20005$ Å. Similar changes of c-parameter were observed in Ref. [37] after thermal annealing in Ar atmosphere of ECD ZnO thin films prepared from hydrogen peroxide precursor on gilded silicon substrate.

According to our data the large lattice deformation was observed for ECD ZnO grown in chloride medium at low temperature (70 °C). From SEM images we could not detect changes for as-grown sample. However, from the values calculated according to the Scherrer formula (Table 1), we observed changes which indicate the lattice deformation.

The texture coefficient for the (0 0 2) orientation was estimated from the following relation [44,58]:

$$TC_{(002)} = \frac{I_{(002)}/I^0_{(002)}}{(1/N)\sum_n I_{(hkl)}/I^0_{(hkl)}}, \quad (11)$$

where $TC_{(0\,0\,2)}$ is the texture coefficient of the (0 0 2) plane, $I_{(h\,k\,l)}$, $I_{(0\,0\,2)}$ are the measured intensities, $I^0_{(hkl)}$, $I^0_{(002)}$ corresponding to recorded intensities according to the JCPDS 036-1451 card [49,54]. N is the reflection number and n is the number of diffraction peaks. A sample with randomly oriented crystallite yields $TC(h\,k\,l) = 1$, while the larger this value, the larger abundance of crystallites oriented at the $(h\,k\,l)$ direction. The calculated texture coefficients TC are presented in Table 1. It can be seen that the highest TC is obtained for the (0 0 2) plane of the ZnO thin film annealed at 150 °C. The variation of texture coefficient of ZnO films annealed at 150 °C and 400 °C are shown in Fig. 3. The higher values of texture coefficient reveal that the zinc oxide film crystallinity is improved

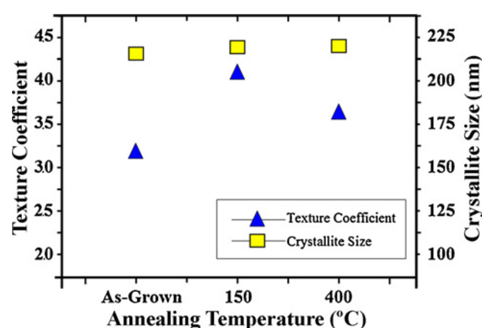

Fig. 3. Variation of the texture coefficient $TC_{(0\,0\,2)}$ and mean crystallite size with thermal annealing temperature of ECD ZnO thin films. Mean crystallite size: as-grown, 2180 Å; 150 °C, 2189 Å; and 400 °C, 2189 Å.

after thermal annealing. This value is comparable with the one inherent to the best ZnO thin films samples [59].

The average crystallite size of the ZnO film was estimated from X-ray diffraction patterns using Scherrer method [53]:

$$d = \frac{K\lambda}{(\beta^2_{obs} - \beta^2_{ins})^{1/2}\cos\theta_B}, \quad (12)$$

where β_{obs} is the measured broadening of a diffraction peak or full-width-half-maximum intensity (FWHM); β_{ins}, the instrumental broadening; K is Scherrer's constant, a unit cell geometry dependent constant; λ, is the wavelength of the X-ray radiation (0.154056 nm) and θ_B is the Bragg diffraction angle. $\beta = (\beta^2_{obs} - \beta^2_{ins})^{1/2}$ is the FWHM of the peak after correcting for peak broadening which is caused by the diffractometer. The crystallite sizes d was determined from the (0 0 2) peak with the Software X'Pert HighScore (by PANalytical B.V.) and are shown in Fig. 3. The crystallite size width d shown in Fig. 3 derived from the Scherrer's formula for all samples.

In the thermal annealed ECD ZnO films the shift of the (0 0 2) peak position to the higher 2θ value with the increase of temperature was noticed. The position of this peak is shifted from 34.34° for as-grown ZnO to 34.42° and 34.47° with the increase of temperature from 150 °C to 400 °C. This shift of the diffraction peak position indicates that films are in a uniform state of stress with tensile components parallel to the c-axis [60,61]. It is well known that several aspects contribute to the strain in the thin films, like intrinsic strain induced by impurities and defects in the lattice, expansion coefficient mismatch between the film and substrate. The stress of the ZnO thin films was estimated using the following formula [62,63]:

$$\sigma = -233 \times 10^9 \left(\frac{c_{film} - c_{bulk}}{c_{bulk}}\right) \text{Pa}, \quad (13)$$

where c_{bulk} is the strain-free lattice constant, and c_{film} is the lattice constant of the film. According to XRD data, the stress value changes from -0.528×10^9 Pa in as-grown sample to -0.134×10^9 Pa in annealed sample. The negative sign indicates that the thin films are in a state of tensile stress. The annealing of the ZnO films leads to the shift of the (0 0 2) peak position to 2θ value equal to 34.467°, which means that the tensile stress is relaxed/relieved due to the rearrangement of atoms in ZnO. It can be observed that after annealing films evolve to a state of compression as compared to the normal lattice state of powder ZnO, which agrees with the angular peak position analysis.

SEM studies were used to inspect surfaces of the as-grown ZnO films and the effect of annealing on the microstructure (Fig. 4). The crystallite sizes were nearly the same for ZnO films before and after annealing, which is in agreement with previously obtained results for ZnO [64].

According to the plane view SEM images of these crystallites (Fig. 4) a diameter value in the range 200–250 nm is estimated. These nanocrystals look like ZnO nanorods material with preferential c-axis perpendicular to the substrate surface. This means that we can see (0 0 2) surface on top view. After annealing at 400 °C, 1 h in air, pin-holes on the surface (0 0 2) and on the lateral facets were observed (Fig. 4f). These pin-holes on the surface and on the sides of ZnO crystallites became larger after thermal annealing at temperatures higher than 600 °C, 1 h in air, and the crystallites have a surprising "Swiss-cheese" aspect (Fig. 4f, down-inset). Comparison of Fig. 4e and f shows that samples annealed at 150 °C for 5 h in air have no surface pin-holes. For ECD ZnO films annealed at temperatures higher than 600 °C, it was observed a larger FWHM XRD (0 0 2) peak [$2\theta = 0.1248^\circ$]. Since these ECD ZnO films annealed at higher temperatures were not in the scope of our work, they were not investigated further. However

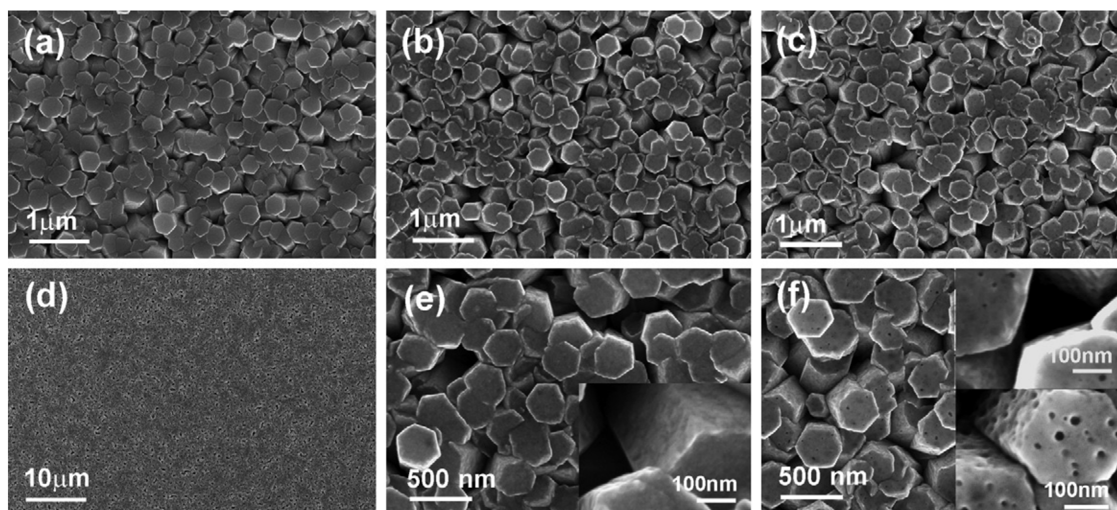

Fig. 4. SEM images of ECD ZnO thin films (plan view) before and after thermal annealing: (a) as-grown; (b) annealed at 150 °C, 5 h in air; (c) annealed at 400 °C, 1 h in air; (d) as-grown (overall view); (e) annealed at 150 °C for 5 h in air (zoom-in), insert shows top and side of a single ZnO crystallite forming film; and (f) annealed at 400 °C, 1 h in air. The upper-insert in (f) shows top and side of a single ZnO crystallite after annealing at temperatures of 400 °C, 1 h. The down-insert is sample after annealing at temperatures higher that 600 °C, 1 h.

discussions related to appearance of these pin-holes on (0 0 2) surface of ZnO crystallite forming zinc oxide film are important. These pin-holes will be discussed below and more detailed elsewhere in a forthcoming paper.

Transmission Electron Microscopy (TEM) was employed to characterize the as-synthesized ZnO thin films and to investigate the effect of annealing on its structure. Samples for TEM analysis were prepared by using FIB as previously described in details [65]. To prepare TEM samples, the ECD ZnO thin films were cut from the substrate by using FIB and mounted on the inside of a TEM Cu-ring by the in-situ lift-out technique in a FIB system [65]. The high-resolution TEM (HRTEM) images from cross-sectional of Pt/ZnO/FTO structure and selective area electron diffraction (SAED)-pattern of ZnO films are shown in Fig. 5, where Fig. 5a is the as-grown film, Fig. 5b is the film annealed at 150 °C for 5 h in air, and Fig. 5c is the film annealed at 400 °C, 1 h in air. For the annealed samples (Fig. 5b and c), columnar grains grown on a FTO substrate are clearly observed. According to SAED, the regular columnar crystalline layer has a crystallographic orientation relationship with the FTO substrate for as-grown and annealed samples. As indexed in the low-right corner of the inset SAED pattern (Fig. 5a), the ZnO is grown along the direction of [0 0 1] zone axis of ZnO, which corresponds with the XRD result. The electron diffraction pattern observed (inset of Fig. 5a) confirms that the ZnO film is highly crystalline with a hexagonal crystal lattice. In the cross-sectional TEM images it can be observed that the entire as-grown ZnO is single-crystalline zinc oxide with a Wurtzite structure grown along the <0 0 2> direction, which is consistent with the XRD results. The SAED pattern (Fig. 5a) reveals that, in this region, the ZnO possess a single-crystal hexagonal structure without dislocations and stacking faults.

The HRTEM image in Fig. 5 shows the crystal structure of the individual ZnO crystallites regular and perpendicular to FTO substrate and their average width of about 200–250 nm. Lines between the individual ZnO grains due to annealing are found at the surface of the film (Fig. 5b and c), which typically extend about half way into the ZnO layer, between ZnO crystallites.

Furthermore, as can be seen from Fig. 5b, the ZnO film also shows in its cross-section some bright spots on regular columnar grains, that means a lower density at these spots. This could be due

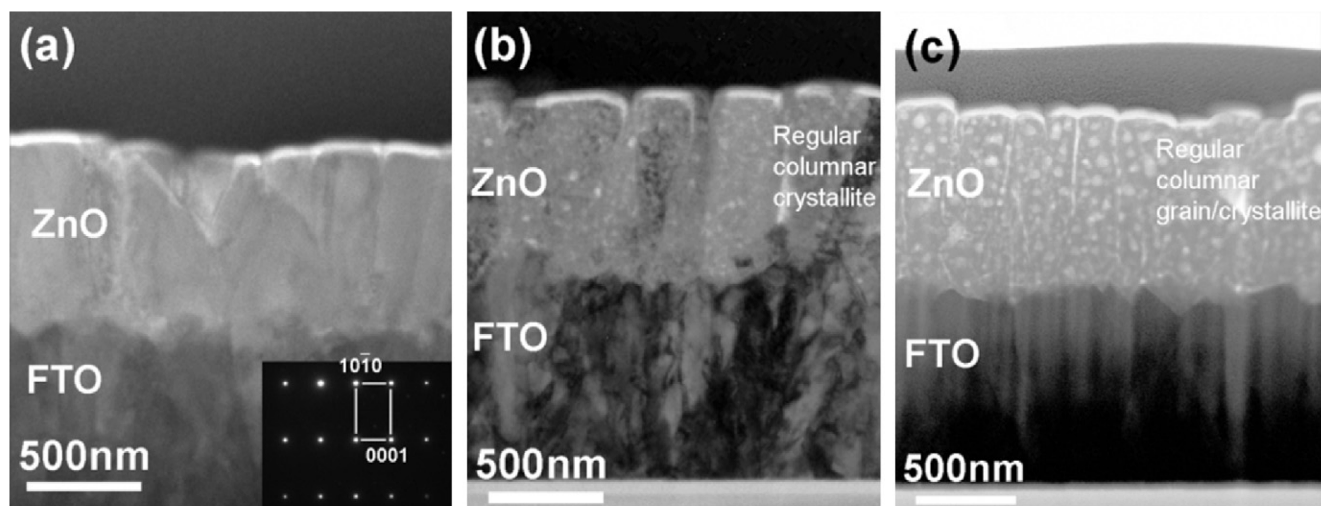

Fig. 5. High-resolution TEM of electrochemical deposited ZnO film on fluor-doped tin oxide substrate (a) as-grown, inset shows selected-area electron diffraction SAED diffraction pattern; (b) annealed at 150 °C for 5 h in air; and (c) annealed at 400 °C, 1 h in air.

to the presence of Cl^-, which may change locally the material density or its response upon FIB milling during the cross-section preparation of TEM sample. The TEM also reveals at sharp edges a very good lattice structure. According to our investigations by TEM and STEM, the chemical compositions of the spots/dots were found to be identical as other locations. Thus, the explanation for such observations could be density changes in ZnO thin film ECD from chloride medium.

It is quite clear that the regular ZnO columnar crystallines grew along *c*-axis and the ZnO film was in 3D-growth. As ZnO has strong ionic bonds, the *c*-axis oriented thin film could grow on the FTO substrate, because surface free energy plays the most important role, compared to the stress or interfacial energy between the ZnO and FTO substrates. By controlling well deposition regimes within the optimum range of the energetically stable state, ZnO thin films have grown with a *c*-axis orientation. These HRTEM data are corroborated with the XRD measurement in our work. It is suggested that for ZnO (0 0 2) orientation, the surface energy reaches a minimum and the growth orientation develops into one crystallographic direction of the lowest surface energy [66]. The (0 0 2) texture of the zinc oxide thin film must form in an effective equilibrium state where enough surface mobility is given to impinging atoms under a certain deposition condition [67].

It is known that the bulk ZnO can be decomposed at about 1950 °C [1,2], for nano-ZnO the decomposition temperature could be lower. Previous reports [50,64] pointed out that there is no change in morphology up to 800 °C. Kim et al. [68] suggested that the reduction of thickness of ZnO films after annealing at 900 °C was due to evaporation. In the current work annealing was performed at relative low temperatures of 150 °C and 400 °C and measurements showed that the thickness of the films remains unchanged at 0.80 μm. It is necessary to mention that the values found for the grain size at three different substrate temperatures are in the range 200–220 nm which is in accordance with observed SEM images (Fig. 4). So, the appearance of nano-holes on the surface of ZnO films after annealing at temperatures higher than 400 °C in air could be due to chlorine incorporation in ZnO and/or possible evaporation of chlorine-based impurities. Chlorine content in the ECD ZnO thin films seems to be a key point to understand the observed morphological changes. In this work several techniques such as EDX, XPS and SIMS have been employed in order to better understand this issue and the distribution of Cl in the ZnO film.

3.2. Chemical characterizations (EDX, XPS and SIMS)

Fig. 6 shows the EDX spectrum of ZnO films electrodeposited on FTO substrate. It can be distinguished Zn, O peaks from the ZnO film, also peak of Sn from the substrate F:SnO_2. The incorporation of chlorine in ZnO films was confirmed by EDX spectra shown in Fig. 6. It can be seen a peak of Cl at 2.63 keV which demonstrates chlorine's presence in the ZnO thin films electrodeposited from chloride medium. Chlorine content in as-grown zinc oxide thin films was found about 3 at%, which is in agreement with previously reported values [35].

The effect of annealing on [Cl]:[Zn] ratio estimated by EDX analysis in ECD ZnO thin films is indicated in Table 1. After annealing at 150 °C, this ratio increases but remains within the uncertainty of the titration method. When samples were annealed at 400 °C, chlorine content slightly decreases (Table 1) and the intensity of the chlorine signal was also lowered in the EDX spectra. According to EDX results, thermal annealing at 400 °C in air contributes to evaporation of about 20% of Cl. These data corroborate with XRD patterns shown in Fig. 2 and lattice parameters calculations above (Table 1). The XRD peak positions shift towards higher angles comparing with position for (0 0 2) in

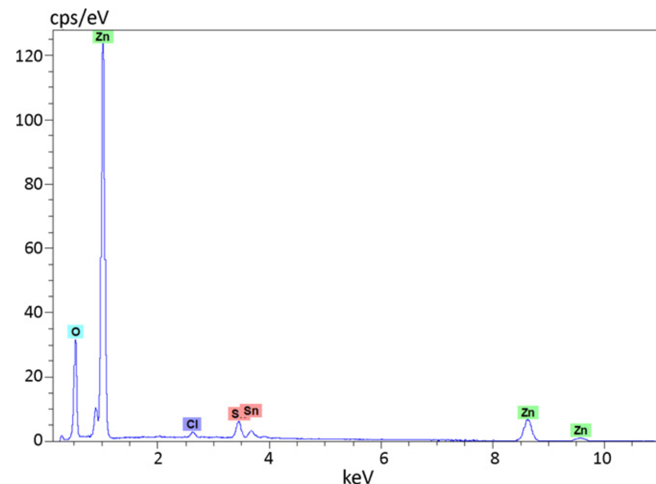

Fig. 6. EDX spectrum of electrodeposited ZnO films on FTO susbtrate from chloride medium.

as-grown sample for the annealed samples. After annealing at 150 °C and at 400 °C (0 0 2) peak shifts, showing a decrease of the lattice parameters (comparing with as-grown ZnO films), which can be corroborated with the rearrangement of the atoms in the lattice at 150 °C and then evaporation of larger Cl ions from ZnO at higher temperature. This result may provide indirect evidence that chlorine is incorporated into the crystal structure, causing the ZnO crystal lattice to expand. Similar evidence was reported for ZnO nanorods by Cui et al. [69], which suggested that the chlorine ions likely substitute for oxygen in ZnO.

In order to localize *Cl* in ZnO thin films electrodeposited in chloride medium one performed high-resolution X-ray Photoelectron Spectroscopy (XPS) and SIMS studies. It is necessary to keep in mind that samples were rinsed with DI water immediately after growth to remove residue chlorine ions from the ZnO film surface. The surface composition of the ZnO thin films was investigated as a function of the annealing temperature. The binding energy (BE) scale was calibrated using the adventitious carbon peak (C-1s) at 285 eV as reference [46,70]. In our samples, residual amounts of adventitious carbon and carbonyl compounds are unavoidable due to their exposure to air prior to the XPS measurements [71].

XPS survey spectra are presented in Fig. 7. The following elements were detected: Zn, O, Cl, and C. No other contaminants from the ZnO film electrodeposition process were observed. Fig. 8 shows XPS spectra of the (a) Zn-2p, (b) O-1s, and (c) Cl-2p core level regions of our samples. The ZnO films display a doublet at 1021.7 eV and 1044.8 eV (vertical reference lines) corresponding to the Zn-$2p_{3/2}$ and $2p_{1/2}$ core levels of ZnO [72,73]. No clear indication of the formation of Zn-Cl compounds can be inferred from the analysis of the Zn-2p XPS region, since higher BEs (∼1023.6 eV) have been reported for $ZnCl_2$ [74]. Nevertheless, the presence of small amounts of Cl in these samples was inferred from our high-resolution XPS analysis of the Cl-2p region, Fig. 8c.

The asymmetric O-1s peak in Fig. 8b, was deconvoluted by four subspectral components corresponding to: (i) ZnO (530.2 eV), (ii) defective ZnO_x and/or Zn-OH species (531.6 eV) [75], (iii) adventitious CO (531.1 eV, dotted line) [76], and (iv) adventitious CO_2 (532.5 eV, dashed-dotted line) [77,78]. Table 2 summarizes the content in at% of each of those species obtained from the XPS spectral fits. Armelao et al. [79] and Liqiang et al. [80] observed similar components in their O-1s spectra and attributed the high BE peak to Zn-OH species. Considering their O-1s/Zn-2p XPS intensity ratios, the $ZnO_x(OH)_y$ stoichiometry was suggested [79]. In our studies, the total O-1s/Zn-2p ratios are: 1.2 (as-grown sample #1) and 1.6 (annealed sample #3). In agreement with our

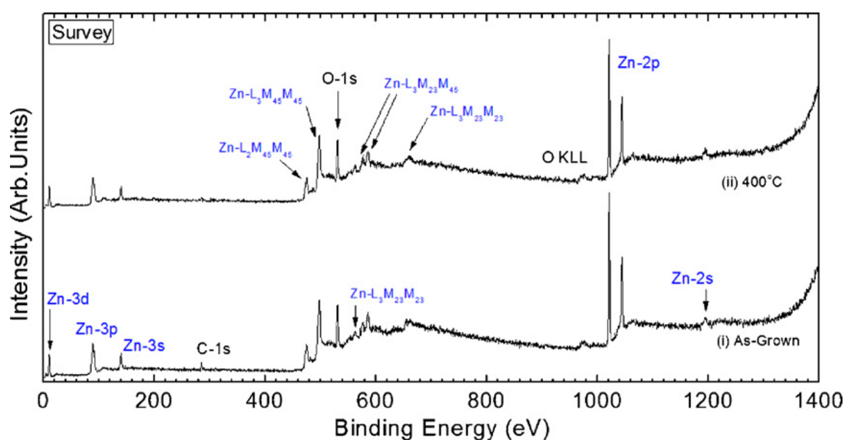

Fig. 7. Survey XPS spectra corresponding to ZnO films supported on glass substrates. Only Zn, O, Cl and adventitious C are detected. The different photoelectron and AES peaks observed for the latter elements are labeled in the graph.

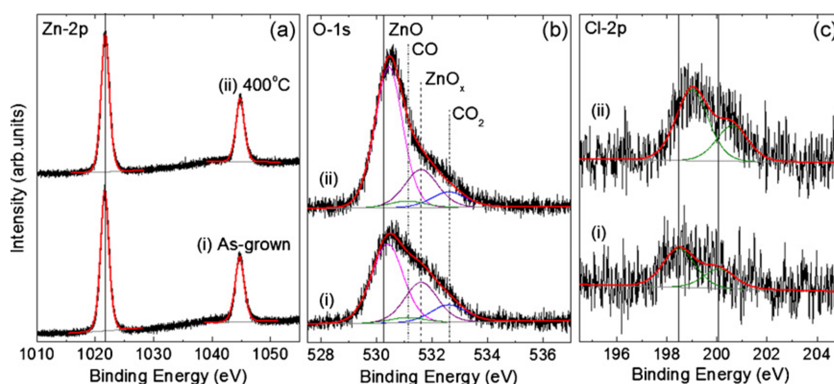

Fig. 8. XPS spectra (Al-Kα = 1486.6 eV) corresponding to the (a) Zn-2p, (b) O-1s and (c) Cl-2p core level regions of ZnO thin films supported on FTO glass substrates.

TEM-EDX data, small Cl signals are observed by XPS in all three samples. These are residual species from our electrodeposition sample preparation method. The Cl-2p region was deconvoluted with 2 spin–orbit doublets (ΔE = 1.6 eV) assigned to the Cl-2p$_{3/2}$ and 2p$_{1/2}$ core levels. Due to the small amount of Cl detected in these samples as well as the proximity of the BEs of different chlorinated species ($ZnCl_2$, Zn_2Cl_4, ZnOCl, etc.) [81], their assignments are challenging.

Fig. 9 shows the Zn^{64}, Cl^{37} and F^{19} isotopic composition depth profiles in the as-grown and annealed (at 400 °C) ZnO/FTO substrate measured by SIMS using the Cs^+ primary beam at a source potential of 3 kV and an impact angle of 60° from normal. The vertical axis showed the count rates of as-deposited and annealed samples for Zn, Cl and F ions. Since no calibration standard was available, the absolute concentration of Cl ions was not obtained in our samples. The depth profile of Cl ions is fairly uniform for the as-deposited ZnO sample (see Fig. 9). However after annealing, the Cl concentration near the surface of ZnO layer is clearly reduced, indicating the loss of chlorine incorporation in ZnO and possible evaporation of chlorine-based impurities ions after thermal annealing at 400 °C.

Fig. 9 demonstrates that annealing at 400 °C modifies SIMS depth profile at the surface region of ZnO film. This confirms the suggestion we have already made based on SEM image (Fig. 3f) related to the appearance of nano-holes voids/dots appeared on the (0 0 2) surface of ZnO after annealing at 400 °C could be due to

Table 2
Relative content of the different Zn-O and C-O species on the surface of our electrodeposited ZnO films extracted from the fits of O-1s XPS spectra.

Sample	ZnO (530.2 eV)	ZnO_x or $ZnO_x(OH)_y$ (531.6 eV)	CO (531.1 eV)	CO_2 (532.5 eV)
(i) As-grown	54.1	28.7	13.3	3.9
(iii) 400 °C	65.6	21.2	9.2	4

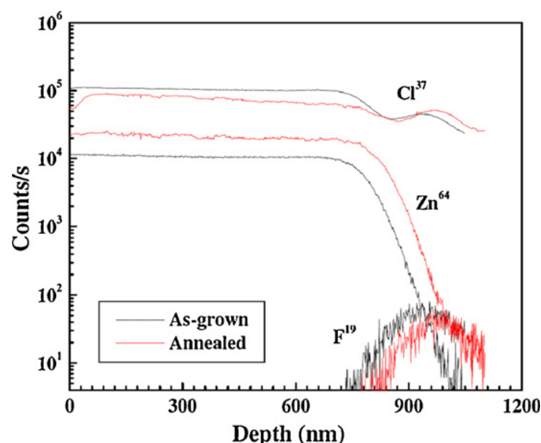

Fig. 9. SIMS depth profiles of as-grown ZnO film electrodeposited on FTO substrate and of annealed at 400 °C (red curve). (For interpretation of the references to color in this figure legend, the reader is referred to the web version of the article.)

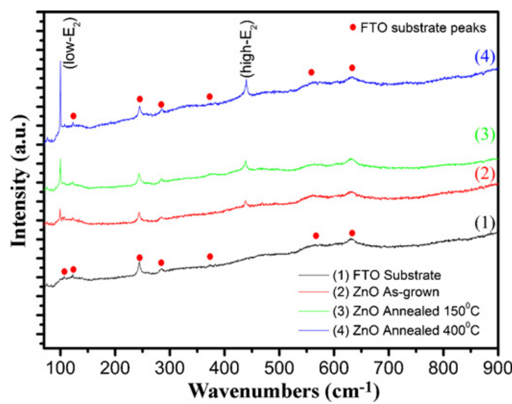

Fig. 10. Raman spectra for as-grown and annealed ZnO thin films on FTO substrate. Curve 1 shows Raman spectra from the FTO substrate. Curves (2) and (3) shows Raman spectra from ZnO films annealed at 150 °C for 5 h in air and at 400 °C for 1 h in air, respectively.

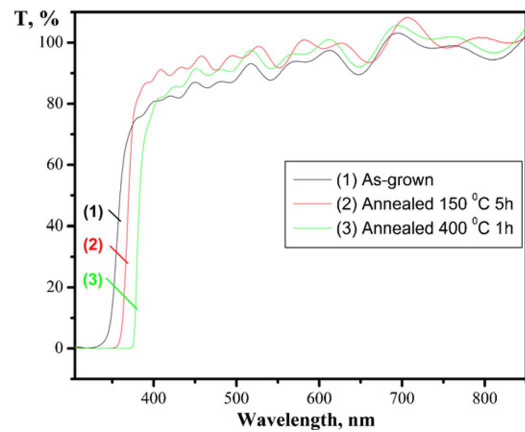

Fig. 11. Transmission spectra of ZnO films as-grown and annealed at 150 °C and 400 °C, respectively.

possible evaporation of chlorine-based impurities ions from ZnO. Also we observe that Cl content decreased in the depth of ZnO sample. These data corraborates with EDX data presented above (Table 1) showing bulk changes in [Cl:Zn] ratio from 0.0319 (as-grown) to 0.0344 (annealed at 150 °C), and to 0.024 (annealed at 400 °C). The decreases in the in-deep Cl content may be due to the evaporation of Cl from the lateral facets of ZnO crystals.

According to data presented in Fig. 9, some diffusion of Cl from ZnO film into the FTO substrate at the ZnO/FTO interface is observed. Such diffusion is indicated by the slope of Cl^{37} curve in annealed sample with respect to the slope of Cl^{37} in the as-grown ZnO near the interface between ZnO and FTO.

3.3. Micro-Raman scattering

Raman measurements provide information about the material quality, the phase and purity, in order to understand transport properties and phonon interaction with the free carriers, which determine the device performances [82]. Considering the ZnO which belongs to the Wurtzite space group $C^4_{6\nu}$, phonon modes E_2 (low and high frequency), A_1 [(TO)-transverse optical and (LO)-longitudinal optical] and E_1 (TO and LO) are expected all being Raman and infrared active. The optical phonons at the Γ point of the Brillouin zone belong to the representation [83]:

$$\Gamma_{opt} = 1A_1 + 2B_1 + 1E_1 + 2E_2 \quad (14)$$

Fig. 10 shows the Raman spectra measured in a backscattering geometry for the as-grown and annealed ZnO thin films ECD on FTO substrate. The Raman spectrum from the FTO substrate itself is presented as a reference (Fig. 10, curve 1). It can be observed that the broad peaks at 106 cm^{-1}, 122 cm^{-1}, 244 cm^{-1}, 284 cm^{-1}, 373 cm^{-1}, 472 cm^{-1}, 494 cm^{-1}, 561 cm^{-1}, and 633 cm^{-1} arise from the FTO substrate and can be found in all spectra of our samples. The noted E_2 (high) peak is one of the characteristic peaks of Wurtzite ZnO attributed to the high frequency E_2 mode [84] assigned to multiple-phonon processes. Dominant peaks at 100 cm^{-1} and 438 cm^{-1}, which are commonly detected in the wurtzite structure ZnO [84,85], are attributed to the low- and high-E_2 mode, respectively of non-polar optical phonons. The Raman spectrum of as-grown ZnO films exhibits a resolved peak centered at 438 cm^{-1} corresponding to high frequency E_2 (high) mode in ZnO [84]. The better observation of the E_2 (high) mode is obtained for annealed samples and indicates that the crystalline quality of the ZnO thin films is improved with annealing. The Raman spectrum of the ZnO films annealed at 400 °C demonstrates the good quality of the Wurtzite crystal structure in the produced material.

All three samples exhibit similar scattering peaks, indicating that they have identical crystal structures as confirmed by XRD. All the scattering peaks are assigned to either ZnO or FTO substrate. The E_2 (high) peak positions shift from 438 cm^{-1} (as-grown sample) to 438.4 cm^{-1} and 439.6 cm^{-1} for the ZnO films annealed at 150 °C and 400 °C in air, respectively. The slightly longer frequency (or wave number) when samples are annealed at 400 °C could be explained by decrease of the chlorine amount in the ZnO film. These results corroborate with EDX, SIMS and XPS data. In addition, the shift in the E_2 (high) Raman peak is believed to be caused by the reduced stress in the ZnO films after annealing at 400 °C, resulting from the substitution of chlorine with oxygen [85]. This result is consistent with the observed lattice parameters changes calculated from XRD measurements. As was discussed above, O^- ions (1.40 Å) have a smaller size than Cl^- (1.81 Å) ions, thus it is obvious that the substitution of Cl^- ions with O^- ions results in an reducing of the lattice constant in ZnO.

The line-width of the peak corresponding to low-E_2 (100 cm^{-1}) mode from annealed samples is about 2.3 cm^{-1} (FWHM is 0.78 cm^{-1}) which is comparable to values reported for high-quality ZnO bulk crystals [86]. Also, the position of the E_2 (high) peak of annealed samples corresponds to the phonon of a bulk ZnO crystal [87] indicating a strain-free state of the electrodeposited thin films.

4. Optical characterizations

Fig. 11 shows optical transmittance spectra of as-grown and annealed at 150 °C and 400 °C ZnO thin films, respectively. Three characteristic spectra in the 300–850 nm range (Fig. 11) are labeled as (1)–(3) for as-electrodeposited and annealed samples (150 °C and 400 °C), respectively. All films exhibit a high transparency in the visible range with a steep increase at an absorption edge. It can be seen that the spectrum of ZnO sample is characteristic of pure ZnO phase with an absorption edge observed at ~3.4 eV that corresponds to the bandgap edge (E_g) for crystalline zinc oxide. By comparing transmission spectra curves (1) and (2) in Fig. 11 corresponding to the as-grown and annealed samples it can be observed that in the annealed samples has an increase of the intensity. For the film annealed at 150 °C (curve (2)), the optical transmittance ($T > 90\%$) in the visible region increases by ~10% compared with as-grown ECD ZnO thin films (curve (1)).

The interference fringes indicate that all the ZnO films had optically smooth surfaces as well as the interface with the FTO substrate is also smooth [87]. The absorption edge shifts to longer wavelength as the annealing temperature increases. For the film annealed at 400 °C, the optical transmittance in the visible region

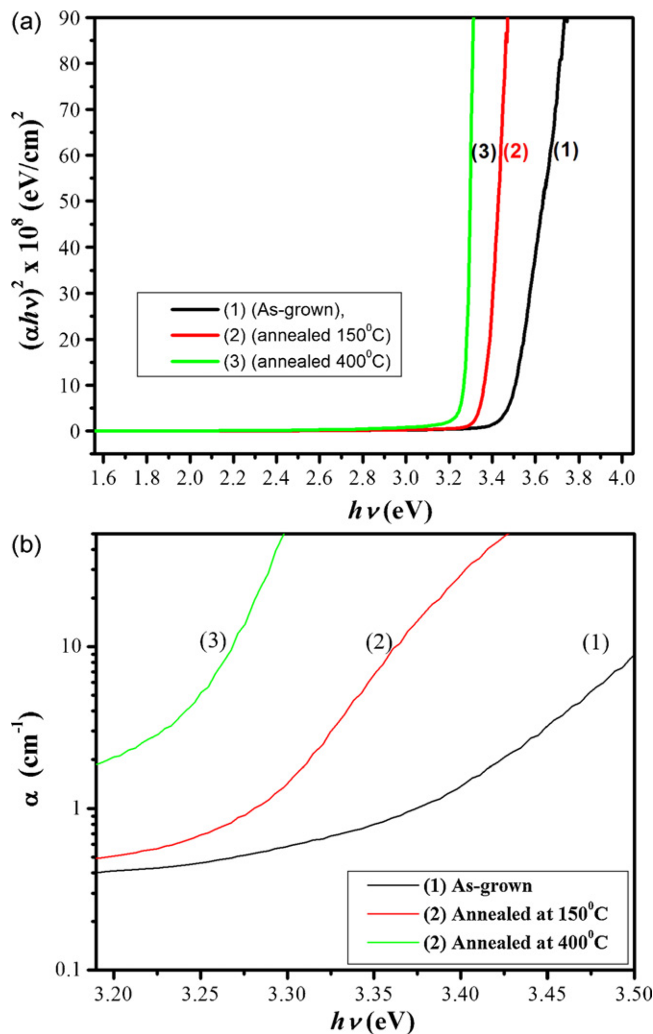

Fig. 12. (a) Plot of $(\alpha\nu h)^2$ vs. photon energy for ZnO films as-grown and annealed at 150 and 400 °C, respectively. (b) Plot of absorption coefficient near the UV edge vs. photon energy ($h\nu$) for ECD ZnO thin films.

decreases by about 15% compared with that of film annealed at 150 °C, probably due to the surface roughness increase observed on these samples.

The optical absorption coefficient was evaluated using Eqs. (3) and (4). The absorption coefficient α strongly depends on the photon energy near the ultraviolet (UV) edge of the ECD ZnO films as shown in Fig. 12a. The energy bandgap (E_g) could be estimated by assuming a direct transition between the valence band (E_V) and the conduction band (E_C) by using the following equation:

$$\alpha h\nu = K(h\nu - E_g)^{1/2}, \tag{15}$$

where K is a constant. The functional dependences of $(\alpha h\nu)^2$ vs. photon energy ($h\nu$) are presented in Fig. 12a. The optical bandgap was found by extrapolating the linear part of curves $(\alpha h\nu)^2$ as a function of incident photon energy $h\nu$ to intercept the Energy x-axis. The optical bandgaps determined from these curves are listed in insert of Fig. 12a.

Although the transmission in the transparent region did not show large changes (about 10–15%), the absorption edge was shifted toward a longer wavelength of about 12 nm (109 meV) by annealing ZnO at 150 °C and of about 22 nm (200 meV) for 400 °C, respectively. As can be seen, the amount of shift is dependent of the annealing temperature and may be attributed to the annealing of intrinsic and extrinsic defects (chlorine may be one of them). The

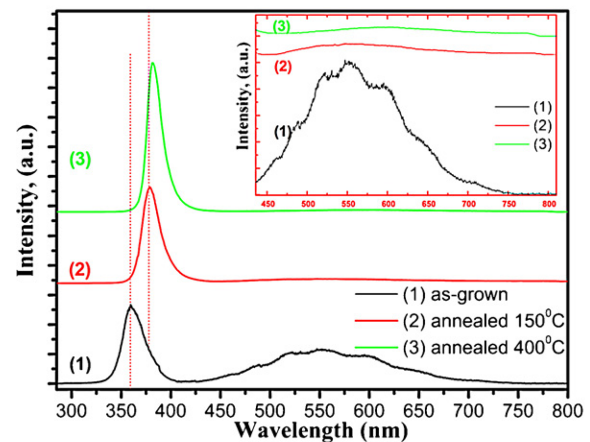

Fig. 13. Photoluminescence spectra of ZnO films electrodeposited on FTO substrate at 70 °C before and after thermal annealing. Insert shows zoom-in visible region of the same PL spectra.

high-E_g of as-grown ZnO films in chloride medium has been assigned to a Burstein–Moss effect, the high value being due to doping [35]. The annealing of defects by thermal treatment induces logically the decrease in donor concentration and the E_g shift towards lower values. It is expected that with increasing annealing temperature, the stoichiometry of the films will be improved and the defects density is decrease [88]. The evaporation of *Cl* may be the way to decrease the donor concentration.

As can be observed from Fig. 12b, the absorption coefficient dependence on photon energy in the spectral range of the near-band-edge empirically follows the exponential law (Urbach tail), which can be expressed as follows [89]:

$$\alpha(h\nu) = \alpha_0 \exp\left(\frac{h\nu}{E_0}\right) \tag{16}$$

where α_0 is a constant, E_0 is an empirical parameter or Urbach energy which corresponds to the width of the band tail and could be determined as the width of the localized states. Usually, E_0 depends on temperature and describes the width of the localized states in the bandgap and could be function of the structural disorder [89,90]. Strickant and Clarke [90] used E_0 to consider effects of all possible defects in ZnO.

Photoluminescence (PL) is a technique which can provide data related to defect levels, and the ratio I_{UV}/I_{DL} (the intensity of the ultraviolet to the visible deep level related luminescence) is a measure of defect states in ZnO material. Fig. 13 shows the room-temperature PL spectra for the studied samples annealed at different temperatures. On the PL spectra, a ultraviolet (UV) emission and a broad visible emission band is observed for the as-grown ECD ZnO film. The UV emission line for the as-grown ZnO films peaking at 361 nm is attributed to a free-exciton and a neutral donor bound exciton. For the annealed samples, the UV exciton-related emission peak is shifted to about 380 nm. So, one can observe a clear shift in UV peak position which increases with the annealing temperature. These results essentially agree with the analysis results of the shift of the optical absorption edge. Thus, the redshift of the optical bandgap and the improved UV emission after annealing can be due to the improved crystallinity of the ECD ZnO film and reduced defects (donor) concentration in the film. It can also be due to Cl^- content reduction in ZnO films after the thermal treatment.

The FWHM values of the UV peaks from as-grown and annealed samples are ranging from 20 nm to 14 nm, respectively. The variation of defects which takes place during the thermal

treatment can be explained as the result of the following reactions [91]:

$$V_O + \frac{1}{2}O_2 = O_O \tag{17}$$

$$Zn_i + \frac{1}{2}O_2 = Zn_{Zn} + O_O \tag{18}$$

where Vo, Zn_i, Zn_{Zn} and O_O are the oxygen vacancy, interstitial zinc, zinc and oxygen at lattice sites, respectively. Relations (17) and (18) indicate that defect concentrations decrease with annealing of ECD ZnO. Therefore the intensity of visible PL emission decreases and UV emission increases, correspondingly. For annealed samples, the visible peak is hardly observed from the insert in Fig. 13. The intensity ratio between the near-band-edge UV emission and the visible is usually used to evaluate the quality of ZnO. This ratio was found equal to 2.3, 33 and 64 for the as-grown sample, for the 150 °C annealed and the 400 °C annealed samples, respectively. We can note that Pauporté et al. [35] have recently shown that as-grown ECD ZnO film of very high quality can be also prepared by carefully choosing the bath composition and the deposition parameters.

According to Fig. 13, the luminescence peaks show a Stokes-shift toward the lower-energy absorption edge. The broader UV PL peak from as-grown sample (Fig. 13, curve 1) and its shift are frequently observed in alloy semiconductors [92], where carriers feel different potentials depending on the local concentration and/or arrangement of the substituting elements [93]. As the Bohr radius of excitons in ZnO is about 18 Å, thus excitons are sensitive to local inhomogeneities [93]. These inhomogeneities could be due to Cl incorporation in ECD ZnO film as was analyzed above.

These results essentially agree with the analysis results of the shift of the optical absorption edge and with data about Urbach energy presented above. Thus, the redshift of the optical bandgap and improved UV emission after annealing can be due to the improved crystallinity of the ECD ZnO film and reduced defects concentration in the film. It could also be due to the Cl^- content reduction in ZnO films as previously discussed in details.

Fig. 14 shows the temperature dependence of the edge emission region for PL spectra of the electrodeposited ZnO films as-grown and after annealing at 400 °C for 1 h in air.

According to the temperature dependence of the UV emission energy shown in Fig. 14 the emission energy decreases as the temperature increases. The temperature dependence of samples is dominated by the transition between the donor bound excitons DX emission at low temperature and the free-exciton (FX) emission at room temperature [see description in Ref. 35]. In the case of as-grown sample (curve 1, Fig. 14), the emission is dominated by the FX emission over the whole temperature range.

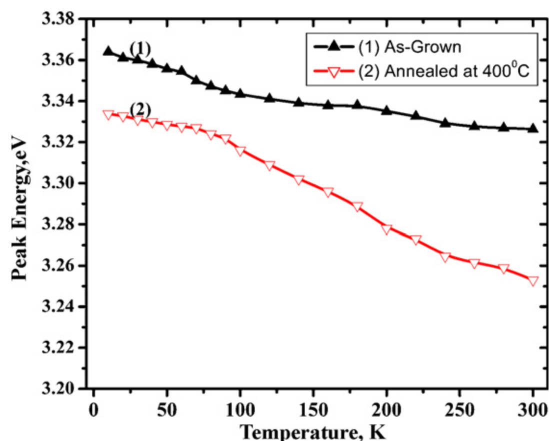

Fig. 14. Temperature dependent UV emission peak position of samples as-grown (1) and annealed at 400 °C (curve 2, red color). (For interpretation of the references to color in this figure legend, the reader is referred to the web version of the article.)

5. Conclusions

ZnO thin films were grown on FTO substrates by the electrochemical method at 70 °C in chloride medium (0.1 M KCl). According to XRD results from the as-grown ECD ZnO film a (0 0 2)-preferred orientation was observed, which suggests that the film is aligned with the *c*-axis oriented perpendicularly to the FTO substrate surface. The effects of low-temperature annealing treatment at 150 °C and 400 °C on the crystallinity, optical transmission, chemical composition and photoluminescence of ZnO thin films electrodeposited on FTO substrates were analyzed. The increase in (0 0 2) diffraction intensity of XRD pattern was observed after annealing at 400 °C. Also, the position of the (0 0 2) peaks is shifted to a higher 2θ values, which could be due to the release of intrinsic strain through annealing. The reasonably narrow FWHM widths in XRD pattern demonstrate the high crystal quality of ZnO films obtained by ECD on FTO substrates. The higher values of texture coefficient reveal that the zinc oxide film crystallinity is improved after thermal annealing. The lattice constants *a* and *c* were determined and one observed an expansion of the lattice parameter. Slightly larger values for both '*a*' and '*c*' parameters in as-grown samples compared to bulk ZnO and annealed samples could be possibly due to Cl^- content or its incorporation in ZnO structure/film.

According to the SEM studies, ZnO thin films are formed from nanocrystals which look like nanorods, with preferential *c*-axis perpendicular to the substrate surface. SEM demonstrates that annealing does not induce significant changes in mean crystallites sizes, which is in accordance with presented XRD data. However, after being annealed at 400 °C, 1 h in air, pin-holes on the surface (0 0 2) and on the lateral facets were observed; which becomes larger after thermal annealing at temperatures higher than 600 °C. Based on SEM and HRTEM results, it is quite clear that the regular ZnO columnar crystallites grew along *c*-axis and the ZnO film was in 3D-growth.

In agreement with our TEM-EDX data, small Cl signals are observed by XPS in all samples. These are species from our electrodeposition sample preparation method. No other contaminants from the ZnO film electrodeposition process were observed. The SIMS depth profile of Cl ions indicate the loss of chlorine incorporation in ZnO and possible evaporation of chlorine-based impurities ions after thermal annealing at 400 °C. This confirms the suggestion we have already made based on SEM image related to the appearance of nano-holes voids/dots appeared on the (0 0 2) surface of ZnO after annealing at 400 °C could be due to possible evaporation of chlorine-based impurities ions from ZnO. Also we observe that Cl content decreased in the depth of ZnO sample.

According to optical characterizations, all films exhibit a high transparency in the visible range with a steep increase of the absorption edge. From the transmission spectra curves corresponding to the as-grown and annealed samples, one can concluded that in the annealed samples, an increase of the optical transmittance intensity ($T > 90\%$) in the visible region by $\sim$10% is obtained as compared with as-grown ECD ZnO thin films. The optical transmission spectra in the transparent region were improved and the absorption edge shifted toward a shorter wavelength side by thermal annealing. The intensity ratio between the near-band-edge UV emission and the visible (which is a good indication of the film quality) was found equal to 2.3, 33 and 64 for the as-grown sample, for the 150 °C annealed, and for the 400 °C annealed samples, respectively.

The characterizations used in this study on as-grown and annealed samples demonstrated that the thermal treatments at

400 °C and 600 °C have an influence on the film morphology due to chloride impurities. They also improved the physical parameters of the electrodeposited ZnO films due to the annealing of intrinsic and extrinsic defects. Finally properties of the ECD ZnO thin films can be very good, which makes this method promising for future applications.

Acknowledgements

Dr. O. Lupan's post-doctoral fellowship and a part of this work was funded by C-nano Ile-de-France program (Project nano-ZnO-LED). Dr. S. Delpech (LECIME) is acknowledged for her help with Raman spectroscopy measurements. The authors are grateful to P. Aschehoug (Laboratoire de Chimie de la Matière Condensée de Paris, ENSCP) for his help in PL measurements. Dr. L. Chow acknowledges partial financial support from Apollo Technologies Inc. and Florida High Tech Corridor Program.

Dr. Roldan Cuenya acknowledges the financial support from the National Science Foundation (NSF-CAREER award, 0448491).

References

[1] H.E. Brown, Zinc Oxide Rediscovered, The New Jersey Zinc Company, New York, 1957.
[2] H.E. Brown, Zinc Oxide Properties and Applications, Pergamon, New York, 1976.
[3] H.E. Brown, J. Phys. Chem. Solids 15 (1960) 86.
[4] R.W. Chuang, R.-X. Wu, L.-W. Lai, C.-T. Lee, Appl. Phys. Lett. 91 (2007) 231113.
[5] Y. Chen, D.M. Bagnall, H.-J. Koh, K.-T. Park, K. Hiraga, Z. Zhu, T. Yao, J. Appl. Phys. 84 (1998) 3912.
[6] (a) R.C. Wang, C.P. Liu, J.L. Huang, S.-J. Chen, Y.-K. Tseng, Appl. Phys. Lett. 87 (2005), 013110;
(b) A. Ohtomo, M. Kawasaki, Y. Sakurai, I. Ohkubo, R. Shiroki, Y. Yoshida, T. Yasuda, Y. Segawa, H. Koinuma, Mater. Sci. Eng. B 56 (1998) 263.
[7] D.C. Look, D.C. Reynolds, J.W. Hemsky, R.L. Jones, J.R. Sizelove, Appl. Phys. Lett. 75 (1999) 811.
[8] C. Coskun, D.C. Look, G.C. Farlow, J.R. Sizelove, Semicond. Sci. Technol. 19 (2004) 752.
[9] (a) A. Burlacu, V.V. Ursakii, V.A. Skuratov, D. Lincot, T. Pauporté, H. Elbelghiti, E. Rusu, I.M. Tiginyanu, Nanotechnology 19 (2008) 215714;
(b) A. Burlacu, V.V. Ursaki, D. Lincot, V.A. Skuratov, T. Pauporté, E. Rusu, I.M. Tiginyanu, Phys. Status Solidi (Rapid Res. Lett.) 2 (2008) 68;
(c) R.E. Peale, E.S. Flitsiyan, C. Swartz, O. Lupan, L. Chernyak, L. Chow, W.G. Vernetson, Z. Dashevsky, Neutron transmutation doping and radiation hardness for solution-grown bulk and nano-structured ZnO, in: Performance and Reliability of Semiconductor Devices, In: M. Mastro, J. LaRoche, F. Ren, J-I. Chyi, J. Kim (Eds.), Materials Research Society Symposium Proceedings 1108, (2009) pp. 55–60.
[10] Ü. Özgür, Ya.I. Alivov, C. Liu, A. Teke, M.A. Reshchikov, S. Dogan, V. Avrutin, S.J. Cho, H.A. Morkoç, J. Appl. Phys. 98 (2005) 041301.
[11] V.A. Karpina, V.I. Lazorenko, C.V. Lashkarev, V.D. Dobrowolski, L.I. Kopylova, V.A. Baturin, S.A. Pustovoytov, A.Ju. Karpenko, S.A. Eremin, P.M. Lytvyn, V.P. Ovsyannikov, E.A. Mazurenko, Cryst. Res. Technol. 39 (2004) 980.
[12] M. Willander, O. Nur, Q.X. Zhao, L. Yang, M. Lorenz, B. Cao, J. Zuniga-Perez, C. Czekalla, G. Zimmermann, M. Grundmann, A. Bakin, A. Behrends, M. Al-Suleiman, A. El-Shaer, A.C. Mofor, B. Postels, A. Waag, N. Boukos, A. Travlos, J. Guinard, S. Dang, D. Le, Nanotechnology (July) (2009).
[13] T. Pauporté, D. Lincot, B. Viana, F. Pellé, Appl. Phys. Lett. 89 (2006) 233112.
[14] G. Chai, O. Lupan, L. Chow, H. Heinrich, Sens. Actuators A: Phys. 150 (2009) 184.
[15] O. Lupan, L. Chow, G. Chai, L. Chernyak, O. Lopatiuk-Tirpak, H. Heinrich, Phys. Status Solidi (a) 205 (2008) 2673.
[16] O. Lupan, S. Shishianu, L. Chow, T. Shishianu, Thin Solid Films 516 (2008) 3338.
[17] (a) O. Lupan, G. Chai, L. Chow, Microelectron. Eng. 85 (2008) 2220;
(b) O. Lupan, L. Chow, G. Chai, Sens. Actuators B: Chem. 141 (2009) 511.
[18] O. Lupan, S. Shishiyanu, V. Ursaki, H. Khallaf, L. Chow, T. Shishiyanu, V. Sontea, E. Monaico, S. Railean, Solar Energy Mater. Solar Cell. 93 (2009) 1417.
[19] T. Yoshida, H. Minoura, J. Zhang, D. Komatsu, S. Sawatani, T. Pauporté, D. Lincot, T. Oekermann, D. Schlettwein, H. Tada, D. Wöhrle, K. Funabiki, M. Matsui, H. Miura, H. Yanagi, Adv. Funct. Mater. 19 (2009) 17.
[20] T. Pauporté, J. Rathousky, J. Phys. Chem. C 111 (2007) 7639.
[21] C. Badre, T. Pauporté, M. Turmine, D. Lincot, Nanotechnology 18 (2007) 365705.
[22] Y.I. Alivov, J.E. Van Nostrand, D.C. Look, Appl. Phys. Lett. 83 (2003) 2943.
[23] R. Perez-Casero, A. Gutierrez-Llorente, O. Pons-y-Moll, W. Seiler, R.M. Defourneau, D. Defourneau, E. Millon, J. Perriere, P. Goldner, B. Viana, J. Appl. Phys. 97 (2005) 054905.
[24] D.C. Oh, T. Suzuki, J.J. Kim, H. Makino, T. Hanada, M.W. Cho, T. Yao, Appl. Phys. Lett. 86 (2005) 032909.
[25] W.Z. Xu, Z.Z. Ye, Y.J. Zeng, L.P. Zhu, B.H. Zhao, L. Jiang, J.G. Lu, H.P. He, S.B. Zhang, Appl. Phys. Lett. 88 (2006) 173506.
[26] D.-K. Hwang, S.-H. Kang, J.-H. Lim, E.-J. Yang, J.-Y. Oh, J.-H. Yang, S.-J. Park, Appl. Phys. Lett. 86 (2005) 222101.
[27] A. Kuroyanagi, Jpn. J. Appl. Phys. 28 (1989) 219.
[28] (a) J.De. Merchant, M. Cocivera, Chem. Mater. 7 (1995) 1742;
(b) P. Nunes, B. Fernandes, E. Fortunato, P. Vilarinho, R. Martins, Thin Solid Films 337 (1999) 176.
[29] Z.B. Shao, C.Y. Wang, S.D. Geng, X.D. Sun, S.J. Geng, J. Mater. Process. Technol. 178 (2006) 247.
[30] H. Khallaf, G. Chai, O. Lupan, L. Chow, S. Park, A. Schulte, J. Phys. D: Appl. Phys. 42 (2009) 135304.
[31] T. Pauporté, D. Lincot, Appl. Phys. Lett. 75 (1999) 3817.
[32] A. Goux, T. Pauporté, J. Chivot, D. Lincot, Electrochim. Acta 50 (2005) 2239.
[33] T. Pauporte, D. Lincot, J. Electroanal. Chem. 517 (2001) 54.
[34] T. Pauporté, D. Lincot, J. Electrochem. Soc. 148 (2001) C310.
[35] T. Pauporté, E. Jouanno, F. Pellé, B. Viana, P. Aschehoug, J. Phys. Chem. C 113 (2009) 10422.
[36] K. Ichinose, T. Yoshida, Phys. Status Solidi (a) 205 (2008) 2376.
[37] K. Laurent, D.P. Yu, S. Tusseau-Nenez, Y. Leprince-Wang, J. Phys. D: Appl. Phys. 41 (2008) 195410.
[38] J. Rousset, E. Saucedo, D. Lincot, Chem. Mater. 21 (2009) 534.
[39] T. Pauporté, R. Cortès, M. Froment, B. Beaumont, D. Lincot, Chem. Mater. 14 (2002) 4702.
[40] T. Pauporté, D. Lincot, Electrochim. Acta 45 (2000) 3345.
[41] E. Chikoidze, M. Nolan, M. Modreanu, V. Sallet, P. Galtier, Thin Solid Films 516 (2008) 8146.
[42] E. Chikoidze, M. Modreanu, V. Sallet, O. Gorochov, P. Galtier, Phys. Status Solidi (a) 205 (2008) 1575.
[43] S. Peulon, D. Lincot, J. Electrochem. Soc. 145 (1998) 864.
[44] Th. Pauporté, Crystal. Growth Des. 7 (2007) 2310.
[45] B.D. Cullity, S. Rstock, Elements of X-ray Diffraction, Prentice Hall, New Jersey, 2001.
[46] O. Lupan, L. Chow, G. Chai, B. Roldan, A. Naitabdi, A. Schulte, H. Heinrich, Mater. Sci. Eng.: B 145 (2007) 57.
[47] H. Francois-Saint-Cyr, E. Anoshkina, F. Stevie, L. Chow, K. Richardson, D. Zhou, J. Vac. Sci. Technol. B 19 (2001) 1769.
[48] J. Pankove, Optical Processes in Semiconductors, Dover Publications, New York, 1971.
[49] Joint Committee on Powder Diffraction Standards, Powder Diffraction File PDF 01-077-0488 card for SnO_2; Powder Diffraction File, Card 36-1451, Joint Committee on Powder Diffraction. Standards, ICDD, Newtown Square (PA) 2001.
[50] X.Q. Wei, Z.G. Zhang, M. Liu, C.S. Chen, G. Sun, C.S. Xue, H.Z. Zhuang, B.Y. Man, Mater. Chem. Phys. 101 (2007) 285.
[51] H.K. Kim, M. Mathur, Appl. Phys. Lett. 61 (1992) 2524.
[52] R.J. Hong, J.B. Huang, H.B. He, Z.X. Fan, J.D. Shao, Appl. Surf. Sci. 242 (2005) 346.
[53] B.D. Cullity, Elements of X-ray Diffraction, 2nd ed., Addison Wesley, 1978.
[54] American Society for Testing and Material, Powder Diffraction Files, Joint Committee on Powder Diffraction Standards, Swarthmore, PA, (1996) pp. 3–888.
[55] T. Tchelidze, E. Chikoidze, O. Gorochov, P. Galtier, Thin Solid Films 515 (2007) 8744.
[56] R.D. Shannon, Acta Crystallogr. A 32 (1976) 751.
[57] CRC Handbook of Chemistry and Physics, 65th ed., CRC/Taylor & Francis, cop. CRC, Boca Raton, FL, 2006.
[58] C.S. Barret, T.B. Massalski, Structure of Metals, Pergamon Press, Oxford, 1980.
[59] (a) J.B. Lee, H.-J. Lee, S.-H. Seo, J.-S. Park, Thin Solid Films 398 (2001) 641;
(b) N.H. Nickel, E. Terukov (Eds.), Zinc Oxide A Material for Micro- and Optoelectronic Applications, Springer, 2004.
[60] H. Deng, J.J. Russell, R.N. Lamb, B. Jiang, Thin Solid Films 458 (2004) 43.
[61] X. Zi-Qiang, D. Hong, L. Yan, C. Hang, Mater. Sci. Semicond. Process. 9 (2006) 132.
[62] Y.G. Wang, S.P. Lau, H.W. Lee, S.F. Yu, B.K. Tay, X.H. Zang, K.Y. Tse, H.H. Hng, J. Appl. Phys. 94 (2003) 1597.
[63] E. Senadin, H. Kavak, R. Esen, J. Phys.: Condens. Matter 18 (2006) 6391.
[64] V.V. Ursaki, O.I. Lupan, L. Chow, I.M. Tiginyanu, V.V. Zalamai, Solid State Commun. 143 (2007) 437.
[65] O. Lupan, L. Chow, G. Chai, H. Heinrich, Chem. Phys. Lett. 465 (2008) 249.
[66] N. Fujimura, T. Nishihara, S. Goto, J. Xu, T. Ito, J. Cryst. Growth 130 (1993) 269.
[67] R.J. Hong, J.D. Shao, H.B. He, Z.X. Fan, Chin. Opt. Lett. 3 (2005) 428.
[68] C.R. Kim, J.Y. Lee, C.M. Shin, J.Y. Leem, H. Ryu, J.H. Chang, H.C. Lee, C.S. Son, W.J. Lee, W.G. Jung, S.T. Tan, J.L. Zhao, X.W. Sun, Solid State Commun. 148 (2008) 395.
[69] J.B. Cui, Y.C. Soo, T.P. Chen, U.J. Gibson, J. Phys. Chem. C 112 (2008) 4475.
[70] V.I. Nefedov, Ya.V. Salyn, G. Leonhardt, R. Scheibe, J. Electron Spectrosc. Rel. Phenom. 10 (1977) 121.
[71] K. Kawase, J. Tanimura, H. Kurokawa, K. Wakao, M. Inone, H. Umeda, A. Teramoto, J. Electrochem. Soc. 152 (2) (2005) G163.
[72] NIST X-ray Photoelectron Spectroscopy Database, version 3.5 (2007), http://srdata.nist.gov/xps/.
[73] B.R. Strohmeier, D.M. Hercules, J. Catal. 86 (2) (1984) 266.
[74] S.H. Jeong, D.-G. Yoo, D.Y. Kim, N.-E. Lee, J.-H. Boo, Thin Solid Films 516 (2008) 6598.
[75] Y. Tak, D. Park, K.J. Yong, J. Vac. Sci. Technol. B 24 (2006) 2047.
[76] K. Tanaka, K. Miyahara, I. Toyoshima, J. Phys. Chem. 88 (1984) 3504.
[77] A.F. Carley, G. Hawkins, S. Read, M.W. Roberts, Top. Catal. 8 (1999) 243.
[78] H. Onishi, Ch. Egawa, T. Aruga, Y. Twasava, Surface Sci. 191 (1987) 479.
[79] L. Armelao, M. Fabrizio, S. Gialanella, F. Zordan, Thin Solid Films 394 (2001) 89.
[80] J. Liqiang, W. Dejun, W. Baiqi, L. Shudan, X. Baifu, F. Honggang, S. Jiazhong, J. Mol. Catal. A: Chem. 244 (2006) 193.
[81] H. Matsuura, F. Tsukihashi, Metall. Mater. Trans. B: Process Metall. Mater. Process. Sci. 37 (2006) 413.
[82] (a) N. Hasuike, H. Fukumura, H. Harima, K. Kisoda, H. Matsui, H. Saeki, H. Tabata, J. Phys.: Condens. Matter 16 (2004) S5807;

(b) W. Limmer, W. Ritter, R. Sauer, B. Mensching, C. Liu, B. Rauschenbach, Appl. Phys. Lett. 72 (1998) 2589.
[83] C. Bundesmann, N. Ashkenov, M. Schubert, D. Spemann, T. Butz, E.M. Kaidashev, M. Lorenz, M. Grundmann, Appl. Phys. Lett. 83 (2003) 1974.
[84] T.C. Damen, S.P.S. Porto, B. Tell, Phys. Rev. 142 (1966) 570.
[85] S.S. Mitra, O. Brafman, W.B. Daniels, R.K. Crawford, Phys. Rev. 186 (1969) 942.
[86] J. Serrano, F.G. Manjon, A.H. Romero, F. Widulle, R. Lauck, M. Cardona, Phys. Rev. Lett. 90 (2003) 055510.
[87] S.T. Tan, B.J. Chen, X.W. Sun, W.J. Fan, H.S. Kwok, X.H. Zhang, S.J. Chua, J. Appl. Phys. 98 (2005) 013505.
[88] S.W. Xue, et al. J. Alloys Compd. 448 (2008) 21.
[89] F. Urbach, Phys. Rev. 92 (1953) 1324.
[90] V. Strikant, D.R. Clarke, J. Appl. Phys. 81 (1997) 6357.
[91] B. Lin, Appl. Phys. Lett. 79 (2001) 943.
[92] R. Zimmermann, J. Cryst. Growth 101 (1990) 346.
[93] S.J. Chen, J. Cryst. Growth 254 (2003) 86.